

Hot UV-bright stars of galactic globular clusters^{★,★★}

S. Moehler¹, W. B. Landsman², T. Lanz³, and M. M. Miller Bertolami^{4,5}

¹ European Southern Observatory, Karl-Schwarzschild-Str. 2, D 85748 Garching, Germany, e-mail: smoehler@eso.org

² Adnet Systems, NASA Goddard Space Flight Center, Greenbelt, MD 20771, USA

³ Observatoire de la Côte d'Azur, F-06304, Nice, France

⁴ Instituto de Astrofísica de La Plata, UNLP-CONICET, Paseo del Bosque s/n, 1900 La Plata, Argentina

⁵ Facultad de Ciencias Astronómicas y Geofísicas, Universidad Nacional de la Plata, Paseo del Bosque s/n, 1900 La Plata, Argentina

Received April 15, 2019 / Accepted May 7, 2019

ABSTRACT

Context. We have performed a census of the UV-bright population in 78 globular clusters using wide-field UV telescopes. This population includes a variety of phases of post-horizontal branch (HB) evolution, including hot post-asymptotic giant branch (AGB) stars, and post-early AGB stars. There are indications that old stellar systems like globular clusters produce fewer post-(early) AGB stars than currently predicted by evolutionary models, but observations are still scarce.

Aims. We wish to derive effective temperatures, surface gravities, and helium abundances of the luminous hot UV-bright stars in these clusters to determine their evolutionary status and compare the observed numbers to predictions from evolutionary theory.

Methods. We obtained FORS2 spectroscopy of eleven of these UV-selected objects (covering a range of $-2.3 < [\text{Fe}/\text{H}] < -1.0$), which we (re-)analysed together with previously observed data. We used model atmospheres of different metallicities, including super-solar ones. Where possible, we verified our atmospheric parameters using UV spectrophotometry and searched for metal lines in the optical spectra. We calculated evolutionary sequences for four metallicity regimes and used them together with information about the HB morphology of the globular clusters to estimate the expected numbers of post-AGB stars.

Results. We find that metal-rich model spectra are required to analyse stars hotter than 40 000 K. Seven of the eleven new luminous UV-bright stars are post-AGB or post-early AGB stars, while two are evolving away from the HB, one is a foreground white dwarf, and another is a white dwarf merger. Taking into account published information on other hot UV-bright stars in globular clusters, we find that the number of observed hot post-AGB stars generally agrees with the predicted values, although the numbers are still low.

Conclusions. Spectroscopy is clearly required to identify the evolutionary status of hot UV-bright stars. For hotter stars, metal-rich model spectra are required to reproduce their optical and UV spectra, which may affect the flux contribution of hot post-AGB stars to the UV spectra of evolved populations. While the observed numbers of post-AGB and post-early AGB stars roughly agree with the predictions, our current comparison is affected by low number statistics.

Key words. Stars: AGB and post-AGB – globular clusters: individual: NGC 5139 – globular clusters: individual: NGC 7099 – globular clusters: individual: NGC 6712 – globular clusters: individual: NGC 6656 – globular clusters: individual: NGC 6121

1. Introduction

Ultraviolet images of globular clusters are often dominated by one or two hot, luminous, UV-bright stars that are more than a magnitude brighter than the horizontal branch (HB) and hotter than 7000 K. Such stars are in various evolutionary stages after helium core burning (HeCB). These evolutionary stages are the most uncertain phases of the evolution of low-mass single stars, caused by uncertainties in the size of the C/O-core due to our poor understanding of convective boundary mixing (Charpinet et al. 2011; Constantino et al. 2015), and our lack of understanding of winds in red giant branch (RGB) stars (McDonald & Zijlstra 2015; Salaris et al. 2016). The previous mass loss on the RGB plays an important role here because it determines whether a star even ascends the asymptotic giant branch (AGB): HB stars with very low hydrogen envelope masses evolve directly from the extreme horizontal branch (EHB, $T_{\text{eff}} \gtrsim 20\,000$ K) to the white dwarf stage, whereas stars with hydrogen envelope masses of more than $0.02 M_{\odot}$ will at least partly ascend the

AGB. Owing to the previous uncertainties, both the masses of the C/O-core and the H-rich envelope of post-HeCB are loosely constrained. In particular, theoretical post-AGB tracks have only been very little tested for old low-mass stars because suitable observations are scarce. A similar situation holds for post-EHB stars that evolve directly to the white dwarf phase and avoid the AGB. As an example, Brown et al. (2008) found far fewer hot post-AGB stars than expected in their Space Telescope Imaging Spectrograph (STIS) UV imagery of M 32, while Weston et al. (2010) reported a similar lack of hot post-AGB stars in the Galactic halo. The status of hot post-AGB stars in globular clusters remains uncertain: with only about one hot post-AGB star per cluster, many clusters must be observed in order to compare number counts, luminosities, and surface gravities with evolutionary tracks.

The detection of hot post-AGB stars in optical colour-magnitude diagrams is limited by selection effects that are caused by crowding in the cluster cores and by the large bolometric corrections for these hot stars. More complete searches are possible for hot post-AGB stars in planetary nebulae, for example, by using O III imaging, as performed by Jacoby et al. (1997) and Bond (2015). The meaningfulness of such searches, however, is limited by the long evolutionary timescales of low-

* Based on observations with the ESO Very Large Telescope at Paranal Observatory, Chile (proposal ID 089.C-0210)

** The extracted spectra, their best-fitting model spectra, and the evolutionary tracks used in this paper will be available at CDS.

mass post-AGB stars, which make the appearance of a planetary nebula unlikely. Only four planetary nebulae have indeed thus far been discovered in the Galactic globular cluster system (Jacoby et al. 1997).

Renzini (1985) and de Boer (1987) first pointed out the advantages of wide-field UV imagery to obtain a complete sample of hot post-AGB stars in a large number of globular clusters. The UV suppresses the dominant cool-star population and emphasizes the hot stars, ensuring that all hot post-AGB stars in the cluster are detected.

Fourteen globular clusters were observed with Ultraviolet Imaging Telescope (UIT, Stecher et al. 1997) in 1990 and 1995 at 1620 Å with a 40' field of view (FOV). Moehler et al. (1998) used ground-based spectroscopy to derive temperatures and gravities of the newly discovered hot UV-bright stars. Their results clearly illustrated the points made above, namely that the HB morphology has a strong influence on the evolutionary status of hot UV-bright stars and that optical selections suffer from a strong bias towards the most luminous hot stars. Subsequently, the Galaxy Evolution Explorer (GALEX) satellite (Martin et al. 2005) was used to obtain wide-field UV images of 41 globular clusters at 1520 Å with a 1.2° diameter FOV. Because GALEX observations are limited by its brightness constraints to mostly high Galactic latitude fields, we obtained archival UV images of an additional 31 clusters using the Swift Ultraviolet-Optical Telescope (UVOT, Poole et al. 2008). The UVOT images are less satisfactory because its FOV is smaller (17'x17') and its wavelength is longer. The solar-blind UVM2 filter on the UVOT has a central wavelength of 2250 Å, while the UVW2 filter has a central wavelength of 1930 Å. The UV imagery from all three wide-field telescopes was complemented by UV imagery with the Hubble Space Telescope (HST, Nardiello et al. 2018), which provides much higher spatial resolution and photometric precision, but rarely encompasses the entire globular cluster within its FOV.

This brings the total number of globular clusters with UV imaging data to 78. Among these, we recovered all previously known hot post-AGB star candidates and found 19 new hot post-AGB star candidates and 16 other new hot stars (mainly apparent EHB or post-EHB stars in globular clusters where only red HB stars have been known so far). Because each cluster contains only a few post-AGB stars, a large sample of clusters is needed to test stellar evolution predictions. To this aim, we started a project to study the whole sample of globular clusters with UV imagery and compare it with stellar evolution predictions. We are currently working on a paper describing the results of this greatly enlarged sample and the new hot post-AGB candidates. As a first step, we describe here the optical spectroscopic observations of 10 of the brightest hot post-AGB star candidates in the Southern Hemisphere and one post-EHB star candidate in M4. The paper is organised as follows. First we describe in Sect. 2 the new observations as well as unpublished data from Moehler et al. (1998), and in Sects. 3 and 4 we derive stellar parameters for all the stars in our sample and discuss some particular cases. This sample is enlarged in Section 5 by including all UV-bright stars that have been studied in previous publications. In Sect. 6 we derive masses from the atmospheric parameters and the distances of the globular cluster, and we discuss the effect of *Gaia* results for some of the closest clusters. In Sect. 7 we then present stellar evolution models of post-HeCB stars at different metallicities and for different masses on the HB and compare simple estimates of the number of luminous hot UV-bright stars predicted by the models with those observed in our sample. Finally, we

end the paper in Sect. 8 with some preliminary conclusions and discuss what needs to be done to improve the comparison.

2. Observations and data reduction

The coordinates and brightness of our targets are listed in Table 1. The data were taken with the FOcal Reducer and low-dispersion Spectrograph 2 (FOR2, Appenzeller et al. 1998) at the ESO Very Large Telescope (VLT) UT1. We used the grism GRIS.1200B with a slit width of 0'5 and verified the resolution from the arc lamp images. The stars in ω Cen (except for ω Cen–UIT151) were observed in multi-object spectroscopy (MOS) mode with movable slitlets of about 20'' length and have a spectral resolution of about 1.7 Å. All other stars (including ω Cen–UIT151) were observed with the long slit with a length of 6'8 and have a spectral resolution of about 1.4 Å. We always took two exposures of each target for consistency checks.

The data were observed between April 1 and July 22, 2012 (date at the beginning of the night). They were processed soon afterwards with the ESO FOR2 pipeline (version fors-4.12.8), except for the flux calibration (see Appendix A). For the bias correction the bias applied to science and calibration data was scaled with the prescan level of these data. In order to take possible structure in the bias into account, the full (prescan-corrected) master bias was subtracted and not just a number. The flat fields were summed per setup and date and normalized using a smoothing with a radius of 10 pixels along both axes. The wavelength calibration used 15 arc lines for the long-slit spectra and 15–17 arc lines for the MOS spectra (depending on the slitlet location). The average accuracy achieved in this way was 0.1 pixel for the long-slit spectra and 0.24 pixel for the MOS data. We used local sky subtraction, that is, fitting of the sky spectrum per slit on the two-dimensional spectra (before rectification and rebinning). Because of the brightness of our targets and the blue wavelength range, the sky level was rather low, even though most of the data were observed while the Moon was above the horizon. To verify the quality of the sky subtraction, we checked our spectra for the presence of G-band features, which should not be present in these hot stars, and found none. The details of the response determination for this volume-phase holographic grism are described in Appendix A.

The extracted spectra showed that NGC 6656–UVBS2 has a close cool fainter neighbour, whose spectrum overlaps with that of the intended target. We did not see any significant lines in the neighbour's spectrum, therefore we smoothed it with a median filter of 14 Å half-width and subtracted it from the spectrum of NGC 6656–UVBS2 (see Fig. 1). In another attempt to avoid the contamination from the cool neighbour we extracted only the part of the spectrum away from the neighbour (marked in red in Fig. 2). The different slopes of the two spectra point towards possible over- and/or undercorrection of the flux from the cool neighbour. The ratio of the two spectra shows no noticeable line residuals. Considering the experience with crowded field spectroscopy recorded in Moehler & Sweigart (2006), we prefer to use the narrowly extracted spectrum for further analysis.

2.1. Unpublished data from Moehler et al. (1998)

After discovering two unpublished spectra (NGC 5139–ROA542 and NGC 5139–ROA3596) from the same observing run as Moehler et al. (1998), we decided to analyse all the data from that observing run again. Based on comments from V. Dixon and P. Chayer, we checked the

Table 1. Target coordinates and brightness.

globular cluster	star	α_{2000} [h:m:s]	δ_{2000} [°:′:″]	m_{UV} [mag]	UV Tel.	V [mag]	Ref
NGC 5139	UIT151	13:27:05.06	-47:21:56.6	15.29 ¹	UIT	16.577	(1)
	UIT644	13:26:44.96	-47:27:09.5	13.12 ¹	UIT	12.713	(1)
	UIT1275	13:26:52.77	-47:29:44.1	14.75 ¹	UIT	14.306	(1)
	UIT1425	13:26:11.56	-47:30:49.2	15.31 ¹	UIT	15.660	(1)
	ROA5342	13:25:45.42	-47:24:02.0	14.73 ¹	UIT	15.944	(1)
	Dk3873	13:26:13.95	-47:25:30.1	15.29 ¹	UIT	16.531	(1)
NGC 6121	UVBS2	16:23:26.25	-26:31:27.0	15.07 ¹	UIT	16.388	(2)
NGC 6656	UVBS2	18:36:22.85	-23:55:19.3	14.88 ²	Swift UVOT	14.533	(3)
NGC 6712	C49	18:53:03.45	-08:42:30.5	17.00 ²	Swift UVOT	16.72	(4)
NGC 6779	ZNG2	19:16:41.28	+30 12 48.5	14.40 ²	Swift UVOT	15.13	(5)
NGC 7099	UVBS2	21:40:18.08	-23:13:22.3	15.54 ³	GALEX	16.75	(6)
Unpublished data from Moehler et al. (1998)							
NGC 5139	ROA542	13:25:49.91	-47:22:59.7	15.33 ¹	UIT	12.876	(1)
	ROA3596	13:27:46.09	-47:30:57.6	14.73 ¹	UIT	14.179	(1)

Notes. ⁽¹⁾ B5 (AB mag, $\lambda_c=1615 \text{ \AA}$, FWHM=225 \AA) ⁽²⁾ W2 (AB mag, $\lambda_c=1928 \text{ \AA}$, FWHM=657 \AA) ⁽³⁾ NUV_AB (AB mag, $\lambda_c=1528 \text{ \AA}$, FWHM=228 \AA)

References. (1) Bellini et al. (2009); (2) Mochejska et al. (2002); (3) Monaco et al. (2004); (4) Cudworth (1988); (5) Rosenberg et al. (2000); (6) Sandquist et al. (1999)

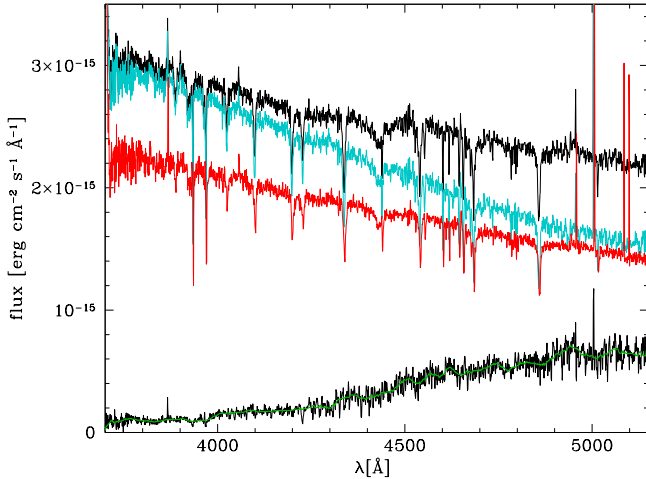


Fig. 1. Flux-calibrated spectra of NGC 6656–UVBS2 and its neighbour (top and bottom black spectra), the smoothed spectrum of the neighbour (green), and the corrected spectrum of NGC 6656–UVBS2 (cyan). The spectrum extracted with narrow limits is marked in red.

resolution of these data and found that the line width used in Moehler et al. (1998) was too high. A pixel scale of $0.336''/\text{pixel}$ and dispersion of $100 \text{ \AA}/\text{mm}$ yield a resolution of 5.6 \AA and not 6.7 \AA , as used by Moehler et al. (1998). The lower value explains most of the differences between the results reported here and those from Moehler et al. (1998).

3. Radial velocities

To correct the observed spectra to laboratory wavelengths, we first corrected to the heliocentric system using the MIDAS command COMPUTE/BARYCOR. Then we determined the radial velocities by fitting Gaussian profiles to the cores of strong lines using the MIDAS command CENTER/GAUSS. We selected the lines and

their fit range manually to ensure that no surviving cosmics or noise peaks distort the results. We did not use lines at wavelengths below 3800 \AA as the bluest arc line in our calibration data is at 3888 \AA . The resulting radial velocities are listed in Table 2, together with the rms error of the individual measurements and the velocities of the corresponding clusters from the literature. The one glaring discrepancy is the radial velocity for NGC 7099–UVBS2 whose value suggests that this star is not a cluster member. This is also supported by the parameters derived in Sect. 4, which argue in favour of a foreground white dwarf.

Two stars with very small formal errors ($\leq 10 \text{ km s}^{-1}$) show velocity differences well above these errors: NGC 6656–UVBS2 ($+33.6 \text{ km s}^{-1}$) and NGC 5139–UIT1275 ($+40.5 \text{ km s}^{-1}$). We recall, however, that one pixel in our data corresponds to 48 km s^{-1} and the resolution of our data corresponds to $90\text{--}120 \text{ km s}^{-1}$. Therefore we decided to consider all stars except for NGC 7099–UVBS2 as members of their respective globular clusters.

4. Atmospheric parameters

Following Moehler et al. (2011) and Brown et al. (2012), we analysed the spectra with grids of non-local thermal equilibrium (NLTE) line-blanketed model atmospheres and NLTE model spectra that were calculated with the NLTE model atmosphere code TLUSTY (Hubeny & Lanz 1995) and the companion spectrum synthesis code SYNSPEC (Hubeny & Lanz 2017). The model atmosphere grids were tailored to the studied sample with the parameter space delimited in Table 3. Over 1100 new model atmospheres have been produced with steps in the model grids of 2000 K in effective temperature, 0.25 dex in surface gravity, and 0.5 dex in helium-to-hydrogen abundance ratio by number, so that the observed spectra can be matched with model spectra that were interpolated from the grids. Scaled-solar abundances based on Grevesse & Sauval (1998) at the cluster’s mean metallicities have been assumed, and kept the same for models with various He/H abundance ratios. The implied change in the total mass fraction of the heavy elements has very limited consequences on our analysis (see Moehler et al. 2011).

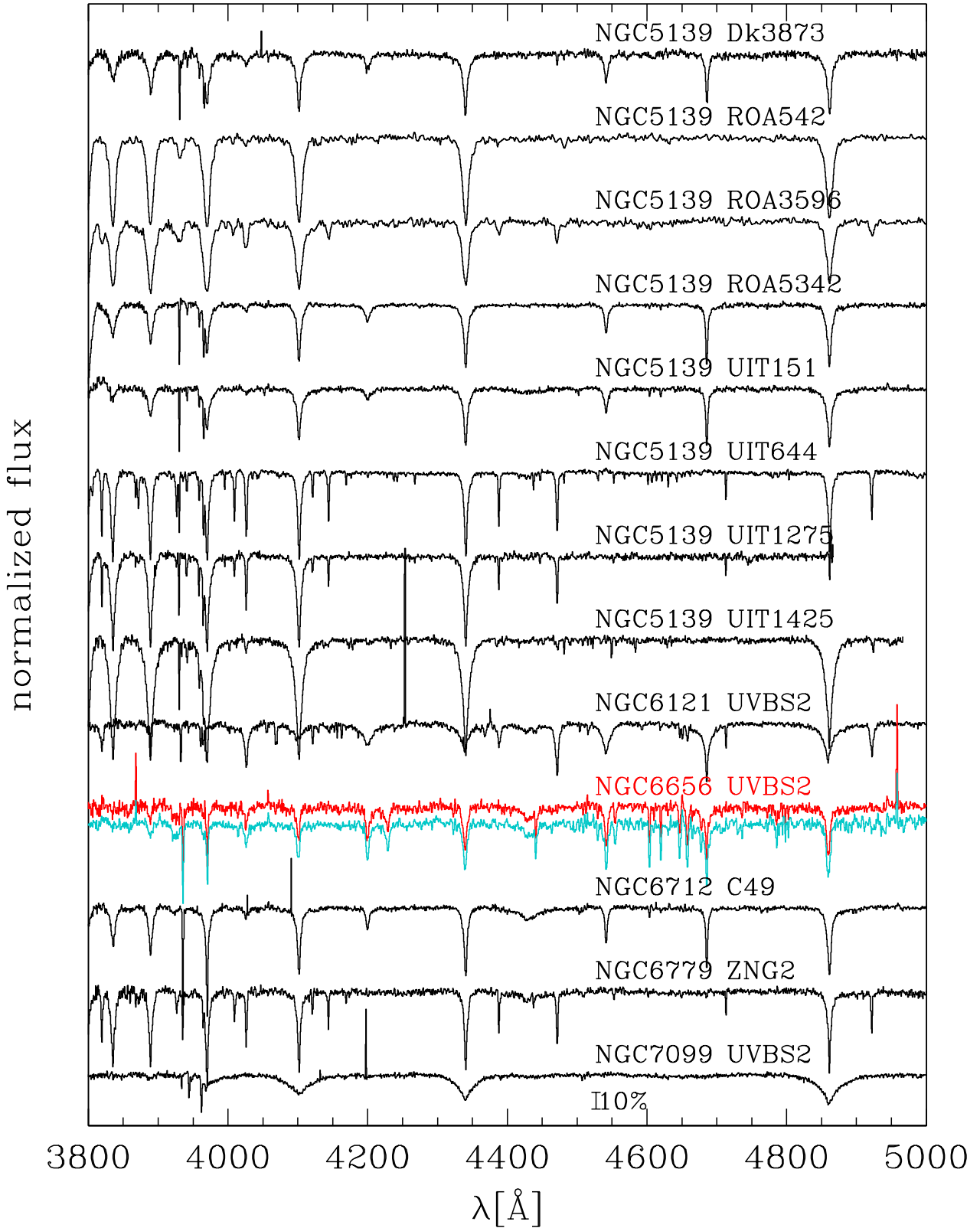


Fig. 2. Normalized spectra. NGC 5139–ROA542 and NGC 5139–ROA3596 are the unpublished spectra from Moehler et al. (1998). For NGC 6656–UVBS2 we show the results of both extraction methods (red marks the extraction within a narrow window, and cyan marks the corrected spectrum, offset by 0.1 along the y-axis). The emission lines for that spectrum are real and due to its planetary nebula.

Table 2. Atmospheric parameters and heliocentric velocities of the stars. The status acronyms are p-AGB (post-AGB), post-early AGB (peAGB), post-HB (pHB), white dwarf merger (WDM), and white dwarf (WD). We have no velocity information for the data from Moehler et al. (1998)

cluster	star	T_{eff} [K]	$\log g$ [cm s ⁻¹]	$\log \frac{n_{\text{He}}}{n_{\text{H}}}$	M [M _⊙]	status	v_{hel} [km s ⁻¹]	n_{ν}	v_{cluster} [km s ⁻¹]	Ref.
NGC 5139	UIT151	62600±2400	5.11±0.10	-0.99±0.08	0.24	peAGB	+231.1±12	9	+231.8	(1)
	UIT644	18000± 800	2.82±0.10	-0.35±0.06	0.29	pAGB	+232.3±13	26		
	UIT1275	17200±1100	3.34±0.18	-1.27±0.18	0.25	pHB	+272.3± 6	14		
	UIT1425	11700± 200	3.57±0.08	-1.72±0.36	0.23	pHB	+213.6±17	9		
	Dk3873	49700±1800	4.99±0.12	-1.21±0.12	0.28	peAGB	+231.2±26	11		
	ROA5342	52000±2000	4.79±0.10	-1.17±0.10	0.29	peAGB	+227.6±10	10		
NGC 6121	UVBS2 ¹	46600± 600	5.82±0.12	+0.89±0.18	0.85	WDM	+74.6±15	17	+71.5	(2)
NGC 6656	UVBS2	78800±9900	4.58±0.20	+0.36±0.16	0.18	pAGB	-111.3± 4	3	-144.9	(2)
NGC 6712	C49 ²	53300±4000	4.50±0.12	-1.04±0.12	0.31	pAGB	-108.0± 8	8	-109.0	(3)
NGC 6779	ZNG2	21500±1800	3.07±0.16	-0.85±0.08	0.19	pAGB	-123.5± 9	15	-138.1	(4)
NGC 7099	UVBS2	65000±2000	7.22±0.12	-3.29±0.12		WD	+11.4± 8	3	-184.4	(2)
Unpublished data from Moehler et al. (1998)										
NGC 5139	ROA542	10600± 200	2.55±0.10	-1.00	0.34	pHB				
	ROA3596	17800±1000	3.56±0.16	-1.26±0.18	0.41	pHB				
New analysis of data from Moehler et al. (1998)										
NGC 2808	C2946	24900±1800	4.78±0.20	-1.88±0.14	0.68	pHB				
	C2947	15000±1200	3.92±0.24	-1.45±0.44	0.41	pHB				
	C4594	19900±1600	3.79±0.22	-1.63±0.26	0.34	pHB				
NGC 6121	Y453	54900±2000	5.62±0.14	-1.25±0.10	0.59	peAGB				
NGC 6723	III60	43000±1400	4.72±0.14	-1.19±0.14	1.02	peAGB				
	IV9	25900±2000	4.02±0.22	-1.06±0.10	0.88	peAGB				
NGC 6752	B2004	34500± 800	5.18±0.14	-2.45±0.24	0.35	pHB				

Notes. ⁽¹⁾ Mochejska et al. (2002) refer to the star as B2 and describe its spectrum as helium rich. ⁽²⁾ Remillard et al. (1980) classified the star as sdO.

References. (1) Johnson et al. (2008); (2) Lane et al. (2010); (3) Yong et al. (2008); (4) Webbink (1981).

The model atmospheres at higher temperature ($T_{\text{eff}} \geq 40\,000$ K) allow for departures from LTE for 1132 explicit levels and superlevels of 52 ions (H, He, C, N, O, Ne, Mg, Al, Si, P, S, and Fe), as in Moehler et al. (2011). A detailed description of the model atoms and the source of the atomic data can be found in Lanz & Hubeny (2003, 2007). Microturbulent velocity is assumed to be $v_t = 5$ km s⁻¹.

At lower temperatures ($T_{\text{eff}} \leq 30\,000$ K), we naturally considered lower ionization stages and excluded some highest ions. The model atmospheres allow for departures from LTE for 1127 explicit levels and superlevels of 46 ions (H, He, C, N, O, Ne, Mg, Al, Si, S, and Fe), with the same sources for model atoms. Microturbulent velocity is assumed to be $v_t = 2$ km s⁻¹. Recently, Dixon et al. (2019) have proposed that setting microturbulence to zero provides a better fit to the spectra of the iron lines in the 21 400 K post-AGB star Barnard 29 in NGC 6205. However, the choice of microturbulence should have little effect on the broad hydrogen and helium lines studied here.

For the cool stars NGC 5139–ROA3596, NGC 5139–UIT1275, and NGC 5139–UIT1425, which are most likely post-HB stars, we used the solar metallicity LTE model spectra described in Moehler et al. (2000) to simulate the effects of radiative levitation. For the re-analysis of the stars cooler than 35 000 K from Moehler et al. (1998) and for NGC 5139–ROA542 we used LTE model spectra like those from Moehler et al. (2000) for metallicities $[M/H] = -1.0$ and -1.5 . For NGC 7099–UVBS2 we used the metal-free NLTE model spectra described in Moehler et al. (1998).

To establish the best fit to the observed spectra, we used the routines developed by Bergeron et al. (1992) and Saffer et al. (1994), as modified by Napiwotzki et al. (1999), which em-

ploy a χ^2 test. The σ necessary for the calculation of χ^2 is estimated from the noise in the continuum regions of the spectra. The fit program normalizes model spectra and observed spectra using the same points for the continuum definition. We fitted the Balmer (and corresponding He II) lines H10 to H β (excluding He ϵ due to the interstellar Ca II absorption line), the He I lines $\lambda\lambda 4026.29$ Å, 4120.81 Å, 4387.59 Å, 4471.60 Å, and 4921.94 Å, and the He II lines $\lambda\lambda 4025.60$ Å, 4199.83 Å (only for stars hotter than 30 000 K), 4541.59 Å, and 4685.68 Å. These fit routines underestimate the formal errors by at least a factor of 2 (Napiwotzki priv. comm.). We therefore provide formal errors multiplied by 2 to account for this effect. In addition, the errors provided by the fit routine do not include possible systematic errors due to flat-field inaccuracies or imperfect sky subtraction, for instance. The results of the line profile fits are listed in Table 2.

For some of the spectra (NGC 5139–UIT151, NGC 5139–Dk3873, NGC 5139–ROA5342, and NGC 6712–C49) we could not fit the H, He I, and He II lines simultaneously because the observed He I lines were weaker than predicted, while the H and He II lines were stronger than predicted. We saw similar effects for NGC 6121–Y453 and NGC 6723–III60 from Moehler et al. (1998). All these stars have effective temperatures between about 50 000 K and 63 000 K and roughly solar helium abundances. A similar behaviour was observed by Latour et al. (2015) for BD+28°4211. They suspected missing opacities to be the cause of the problem. They showed that the effects of increasing metallicity on the hydrogen and helium lines saturate at $[M/H] = +1$ and therefore used model atmospheres with $[M/H] = +1$ for their analysis. With these model atmospheres, they were able to reconcile the parameters derived from optical spectra with those derived

Table 3. Parameter space of metal-poor NLTE TLUSTY model spectra

Clusters	[M/H]	T_{eff} [kK]	$\log g$	$\log \frac{n_{\text{He}}}{n_{\text{H}}}$	v_t [km s ⁻¹]	Number of models
NGC 6121 & NGC 6712	-1.0	40–70	4.00–6.00	-1.5...+1.0	5.	256
NGC 5139 & NGC 6656	-1.5	40–82 16–28	4.25–6.00 2.75–5.75	-3.0...+0.5 -3.0... 0.0	5. 2.	426 332
NGC 6779	-2.0	18–24	2.75–3.25	-1.0...-0.5	2.	24
NGC 7099	-2.3	50–60	5.50–6.75	-3.0...-2.0	5.	108

from UV spectra. We therefore decided to follow the same path and analysed our hotter stars with very metal-rich model spectra. For the synthetic spectra we included only hydrogen and helium lines, as the high metallicity may only be a proxy for missing opacities (see, however, Sect. 4.3 and Fig. 3 for further information). The new results are listed in Table 4. For NGC 6121–Y453 we note that Dixon et al. (2017) obtained similar parameters from the same optical spectrum, but a much higher temperature of 72 000 K (with $\log g$ of 5.7) from far-ultraviolet (FUV) data. For reasons of consistency, we use the value derived here for further discussion.

The effective temperatures clearly decrease and the surface gravities increase with the metal-rich model atmospheres. This effect is also known for cooler stars (e.g. Moehler et al. 2000).

4.1. NGC 6656–UVBS2

The analysis of NGC 6656–UVBS2 was difficult for two reasons: It has a cool neighbour very close by, and it has a planetary nebula. The first results using model spectra with the cluster abundance pointed towards a temperature of almost 80 000 K, while the results obtained with metal-rich model spectra suggest a much cooler temperature of 62 000 K. Based on a low-resolution spectrum, Harrington & Paltoglou (1993) suggested an effective temperature of 75 000 K from the similarity to the sdO star KS 292, which had been analysed by Rauch et al. (1991). The spectrum shows absorption lines of C iv and N v similar to the star SDSS J155610.40+254640.3 (Reindl et al. 2016), which has a temperature of about 100 000 K. The deeper He II lines of NGC 6656–UVBS2 are consistent with a lower temperature, which unfortunately does not allow us to distinguish between the two temperatures mentioned before.

Muthumariappan et al. (2013) suggested that NGC 6656–UVBS2 is the result of a stellar merger. Interestingly enough, SDSS J155610.40+254640.3 was classified by Reindl et al. (2016) as a PG 1159 star, a class of H-deficient post-AGB stars. In any case, it seems that NGC 6656–UVBS2 is closely related to the star ZNG1 in NGC 5904 (see Table 6), which has also been connected to both a merger and PG 1159 stars (Dixon et al. 2004). While NGC 5904–ZNG1 shows a high rotational velocity of about 170 km s⁻¹, we see no evidence for fast rotation in our spectrum of NGC 6656–UVBS2. We recall, however, that the resolution of our data is about 100 km s⁻¹.

4.2. Metal lines

We took care to verify that potential metal lines were present in both individual spectra for each star. We found potential metal lines only in the stars listed below and compared their strength to that predicted by the best-fitting model spectrum. The number of lines for each ion are given in parentheses, and the stars are sorted by evolutionary stage. A detailed abundance analysis is beyond the scope of this paper.

NGC 5139–UIT1425 (pHB) Mg II (1) significantly weaker than predicted by the metal-rich model spectrum with metal lines, which is usual for HB stars in this temperature range.

NGC 5139–UIT151 (peAGB) N v (2) in agreement with the metal-rich model spectrum with metal lines, which also predicts strong C III and O IV lines that are not observed, however.

NGC 5139–UIT644 (pAGB) N II (9), C II (1) Mg II (1), and Si III (2) much stronger than predicted by the metal-poor model spectrum used for the analysis, especially N II.

NGC 6656–UVBS2 (pAGB) C IV (3), N v (2), much stronger than predicted by the model spectrum with metal lines for [M/H] = +1.

NGC 6121–UVBS2 (WDM) C III (7), much stronger than predicted by the model spectrum with metal lines for [M/H] = +1.

4.3. UV spectrophotometry

Several of our targets have archival UV spectra from either the International Ultraviolet Explorer (IUE), the Far Ultraviolet Spectroscopic Explorer (FUSE), or the HST. We defer a complete discussion of the UV spectra to a subsequent paper, but discuss here some of the IUE and HST Faint Object Spectrograph (FOS) data in ω Cen (Table 5), which (1) provide additional justification for our use of metal-rich atmospheres for the sdO stars, and (2) provide evidence of binarity for the star UIT1425. The data were obtained from the Mikulski Archive for Space Telescope (MAST), and the IUE spectra were converted into the HST absolute calibration scale using the transformation in Bohlin & Bianchi (2018). We restricted use of the IUE data to the short-wavelength (< 1950 Å) prime (SWP) camera because the IUE large (10''×20'') aperture includes light from background red stars at longer wavelengths. We expect the SWP images to be free of background contamination because examination of the UIT 1620 Å image of ω Cen showed that no UV sources are included within the IUE aperture for any of the target stars. In addition, the FOS and IUE spectra of UIT151 show fair agreement in Fig. 3, even though the FOS data use a much smaller (1'' circular) aperture.

The high-resolution study of field sdO stars by Latour et al. (2018) showed that the UV spectrum of these stars is dominated by numerous lines of iron and nickel. Even though our low-resolution UV spectra cannot individually resolve these lines, the lines are sufficiently numerous at high metallicity to affect the apparent continuum. Figure 3 shows surprisingly good agreement between the low-resolution UV spectra of the three sdO stars and models with [M/H] = +1.0. The C IV doublet near 1550 Å appears much weaker than predicted by the metal-rich models, suggesting that the light elements do not follow the abundance enhancement seen in iron and nickel, an effect also seen in some field sdO stars (Latour et al. 2018). We are able to use the known metallicity spread of ω Cen to set an upper

Table 4. Atmospheric parameters for stars hotter than 40 000 K derived using model atmospheres with $[M/H] = +1$.

cluster	star	T_{eff} [K]	$\log g$ [cm s ⁻²]	$\log \frac{n_{\text{He}}}{n_{\text{H}}}$	M [M_{\odot}]
NGC 5139	UIT151	57400±2200	5.37±0.08	-1.07±0.08	0.51
	Dk3873	47900±1200	5.15±0.08	-1.19±0.08	0.42
	ROA5342	49800±1400	4.98±0.08	-1.15±0.06	0.46
NGC 6121	UVBS2	46200± 400	5.92±0.12	+0.96±0.14	1.06
NGC 6656	UVBS2	62300±9600	4.59±0.16	+0.40±0.18	0.31
NGC 6712	C49	47800±1800	4.64±0.08	-1.10±0.08	0.51
New analysis of data from Moehler et al. (1998)					
NGC 6121	Y453	56500±1800	5.71±0.12	-1.16±0.10	0.79
NGC 6723	III60	42300±1400	4.80±0.12	-1.13±0.12	1.19

Table 5. Ultraviolet spectra of stars in ω Cen

Star	Telescope	Mode	ID	Date	Exp [s]
UIT151	HST/FOS	G160L	Y2SS402T	1996-04-28	2400
UIT151	IUE	SWP	54154	1995-03-16	23400
Dk3873	IUE	SWP	48271	1993-07-31	19200
ROA5342	IUE	SWP	54333	1995-04-08	25500
UIT1425	IUE	SWP	54804	1995-05-31	26820

limit of $[M/H] = -1.0$ for the metallicity of the progenitors of these sdO stars. The factor of ≈ 100 enhancement in iron and nickel must then be attributed to radiative levitation (Latour et al. 2018).

For NGC 5139–UIT1425 a model spectrum with the parameters derived from our optical spectra cannot reproduce the UV data (see Fig. 4). This star is most likely a binary, as its optical colours ($B - V = -0.01$, $V - I = +0.20$) are appropriate for a blue HB star, whereas its $UV - V$ colour and steep IUE spectrum is more indicative of an sdO star. The optical spectrum, however, shows no trace of He II, which would be a clear sign of the hotter star. Unfortunately, there is no HST imagery in this region of ω Cen, so that we cannot rule out that the binary is a chance alignment. We checked the spatial (line by line) IUE image, but found no presence of more than one star within the large aperture.

5. Data from the literature

In Table 6 we list the physical parameters published for hot UV-bright stars other than those discussed here. For NGC 6656–II-81 we note that its position in the T_{eff} , $\log g$ diagram is consistent with being a post-AGB instead of a post-HB star.

We wish to compare results between different globular clusters, therefore we decided to use homogeneous data sets for their ages (Marín-Franch et al. 2009), metallicities (Carretta et al. 2009), and integrated V magnitudes (van den Bergh et al. 1991). Unfortunately, we found no such data set for the distances and reddenings. Therefore we used the values from Harris (1996) that are at least created in a defined way from the various sources. The values we used in our analysis are listed in Table 7.

6. Masses and distances

Using the atmospheric parameters together with the observed brightness of the stars and reddening and distances to their parent globular cluster, we determined masses using Eq. 1,

$$\log \frac{M}{M_{\odot}} = \log \frac{g_{*}}{g_{\odot}} - 4 \cdot \log \frac{T_{*}}{T_{\odot}} - \frac{M_V + BC - 4.74}{2.5}, \quad (1)$$

which can be rewritten to

$$\log \frac{M}{M_{\odot}} = \log g_{*} + 0.4 \cdot [(m - M)_0 - V_{*} + A_V - BC] - 4 \cdot \log T_{*} + C3, \quad (2)$$

with

$$C3 = -\log g_{\odot} + 4 \cdot \log T_{\odot} + \frac{4.74}{2.5}, \quad (3)$$

with the bolometric corrections from Flower (1996). The results are listed in Tables 2 and 6 and plotted in Fig. 5.

From stellar evolution we would generally expect masses of $0.5 M_{\odot}$ to $0.6 M_{\odot}$. Figure 5 shows that the masses derived for stars below 25 000 K tend to be too low, while the masses derived for hotter stars scatter towards too high masses¹.

Some of the globular clusters discussed in this paper are close enough to have parallax estimates from the *Gaia* DR2 (Gaia Collaboration et al. 2018). The Gaia collaboration compared the parallaxes derived from the *Gaia* measurements to those listed in Harris (1996) and found a systematic difference of 0.029 mas, with the *Gaia* parallaxes being smaller. We therefore used the reported *Gaia* parallaxes only for those clusters that had parallax values of more than 0.23 mas, that is, about eight times the systematic offset. To derive distances, we applied the

¹ The dust in the planetary nebula IRAS 18333–2357 surrounding NGC 6656–UVBS2 (at about 62 000 K) probably provides additional extinction so that the derived mass is definitely a lower limit. Harrington & Paltoglou (1993) estimated a reddening of $E_{B-V} = 0.54$ compared to a global reddening of 0.34 used for the mass determination. This would increase the mass by some 80%, leading to a mass of $\sim 0.55 M_{\odot}$, which is typical of low-mass central stars of planetary nebulae.

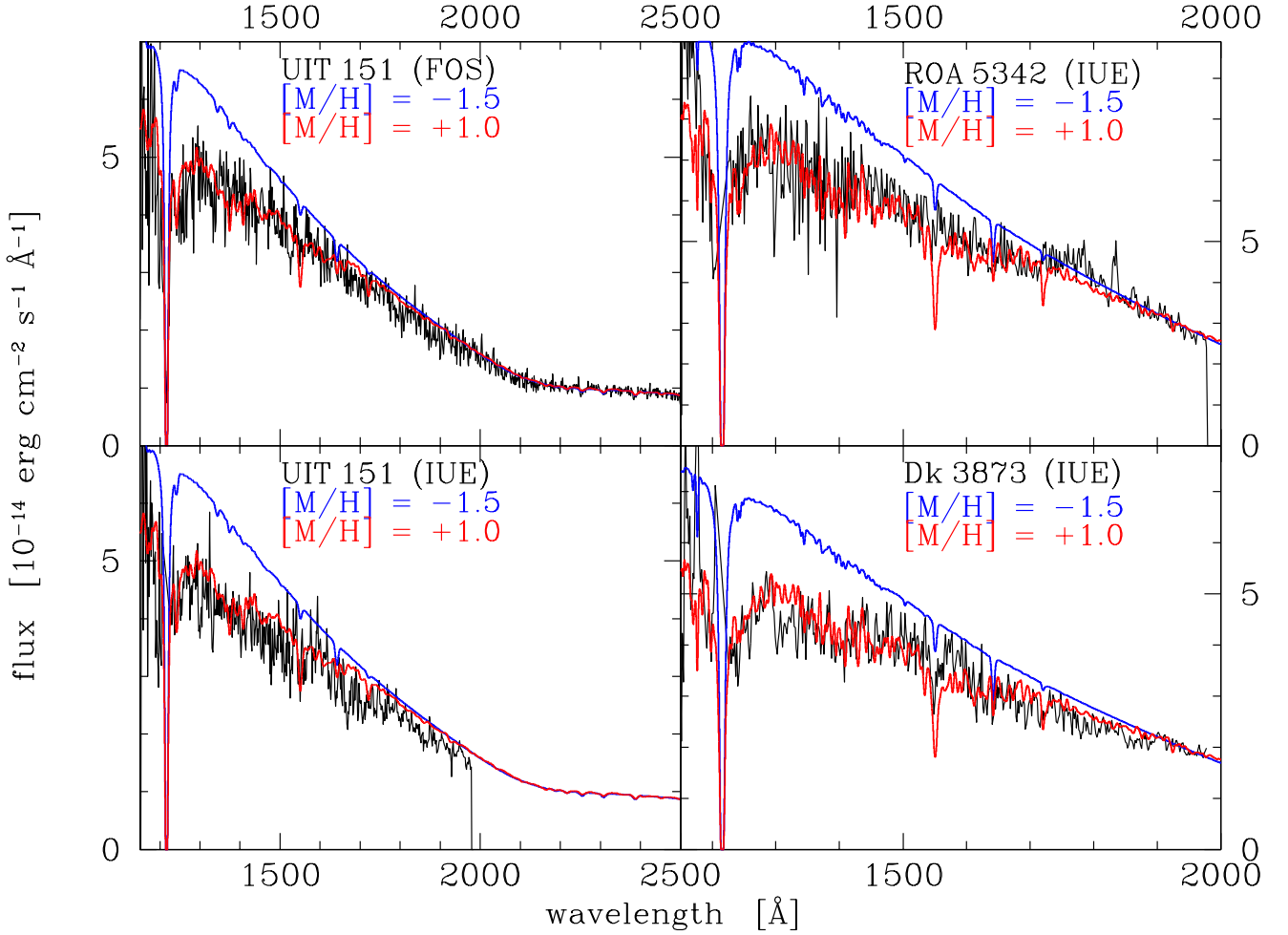


Fig. 3. FOS (UIT151, top left) and IUE (UIT151, ROA5342, and Dk3873) spectra together with model spectra for $[M/H] = -1.5$ (blue) and $[M/H] = +1.0$ (red). The model spectra were calculated for the temperature, surface gravity, and helium abundance listed in Table 4. They were reddened by $E_{B-V} = 0.13$ and aligned to a radial velocity of $+232 \text{ km s}^{-1}$. The model spectra were scaled to the observed flux between 2400 \AA and 2500 \AA in the FOS spectrum and between 1900 \AA and 1950 \AA in the IUE spectra. Metal-rich model spectra are clearly needed to reproduce the observed UV flux.

reported systematic offset to the parallaxes. We then added interstellar extinction as $3.2 \cdot E_{B-V}$. The apparent distance moduli derived that way are 0.29 mag smaller for NGC 6121 and 0.16 mag, 0.18 mag, and 0.08 mag larger for NGC 6397, NGC 6656, and NGC 6752, respectively, than those from Harris (1996). It is interesting to note that we find higher-than-expected masses for the two stars in NGC 6121, which would be reduced by 30% with the *Gaia* distance to $0.81 M_{\odot}$ and $0.65 M_{\odot}$, respectively. For NGC 6397, using the *Gaia* distance would increase the masses by 16%, moving them from about $0.5 M_{\odot}$ to about $0.6 M_{\odot}$. For NGC 6656, using the *Gaia* distance would increase the mass of NGC 6656–UVBS2 from $0.31 M_{\odot}$ to $0.38 M_{\odot}$ (without the additional reddening correction) and from $0.55 M_{\odot}$ to $0.65 M_{\odot}$ (with the additional reddening correction). The change of 8% for the masses of the stars in NGC 6752 is negligible.

7. Stellar evolution models and evolutionary fluxes

The hot UV-bright phase contains stars in different evolutionary stages. The most luminous of these stars ($L/L_{\odot} \gtrsim 3.1$) are

believed to be post-AGB stars, which go through a luminous UV-bright phase as they leave the AGB and move rapidly toward their final white dwarf state. Despite their short lifetimes ($\lesssim 10^5 \text{ yr}$), hot post-AGB stars ($T_{\text{eff}} > 7000 \text{ K}$) can dominate the total UV flux of an old stellar population. UV-bright stars with luminosities $2.65 \lesssim \log(L/L_{\odot}) \lesssim 3.1$ are a mixture of low-mass post-AGB stars, which are stars that departed from the AGB before the beginning of the thermal pulses (post-early AGB stars), and post-EHB stars that managed to ignite the H-burning shell after the departure from the HB, but never reached the AGB. The post-early AGB population arises from hot HB stars with sufficient envelope mass to return to the AGB, but which peel off the AGB prior to the thermally pulsing phase (Dorman et al. 1993). Less luminous hot UV-bright stars ($1.8 \lesssim \log(L/L_{\odot}) \lesssim 2.65$) are mostly evolving from the EHB to the white dwarf domain (post-EHB stars), but some may also evolve from the hot end of the blue horizontal branch (**BHB**) to the AGB phase. The population of post-EHB stars is expected to be about 15–20% of the population of EHB stars (Dorman et al. 1993).

Table 6. Atmospheric parameters of hot UV-bright stars from refereed publications until 2019-03-01. The masses were derived by us as described in Sect. 6.

cluster	star	T_{eff} [K]	$\log g$ [cgs]	$\log \frac{Z_{\text{He}}}{Z_{\text{H}}}$	status	Ref.	V [mag]	Ref.	M [M_{\odot}]
NGC 104	BS	11000	2.5	-1	pAGB	(1)	10.73	(13)	1.25
NGC 1851	UV5	16000	2.5	-1	pAGB	(2)	13.26	(14)	0.41
NGC 5139	ROA5701	25000	3.3	-1	pAGB	(3)	13.13	(24)	0.32
NGC 5272	vZ1128	36600	3.95	-0.84	peAGB	(4)	15.03	(15)	0.41
NGC 5904	ZNG1	44300	4.3	+0.52	pAGB	(5)	14.54	(16)	0.72
NGC 5986	ID6	8750	2.0	-1.4	pAGB	(12)	12.65	(22)	1.21
NGC 6205	B29	21400	3.10	-0.89	pAGB	(6)	13.116	(23)	0.38
NGC 6254	ZNG1	27000	3.6	-1.33	pAGB	(7)	13.23	(17)	0.59
NGC 6397	ROB162	51000	4.5	-1.0	pAGB	(8)	13.1	(9)	0.50
NGC 6656	II-81	38000	4.2	—	pHB	(9)	14.0	(18)	0.47
NGC 6712	ZNG1	11000	2.1	-1.19	pAGB	(7)	13.33	(19)	0.35
NGC 6752	B852	39000	5.2	-2.0	pHB	(10)	15.91	(20)	0.52
	B4380	32000	5.3	-2.3	pHB	(10)	15.93	(20)	0.79
	B1754	40000	5.0	-1.52	pHB	(10)	15.99	(20)	0.30
NGC 7078	K648	39000	3.9	-1.10	pAGB	(11)	14.73	(11)	0.62
	K996	11500	2.5	—	pHB	(12)	14.31	(21)	0.26
	ZNG1	28000	3.7	-1.22	pAGB	(7)	14.8	(17)	0.55

References. (1) Dixon et al. (1995); (2) Dixon et al. (1994); (3) Thompson et al. (2007); (4) Chayer et al. (2015); (5) Dixon et al. (2004); (6) Dixon et al. (2019); (7) Mooney et al. (2004); (8) Heber & Kudritzki (1986); (9) Glaspey et al. (1985); (10) Moehler et al. (1997); (11) Rauch et al. (2002); (12) Jasiewicz et al. (2004). (13) Lloyd Evans (1974) (14) Walker (1992) (15) Buzzoni et al. (1992) (16) Piotto et al. (2002) (17) de Boer (1987) (18) Arp & Melbourne (1959) (19) Cudworth (1988) (20) Buonanno et al. (1986) (21) Buonanno et al. (1983) (22) Alves et al. (2001) (23) Sandquist et al. (2010) (24) Bellini et al. (2009)

Table 7. Metallicities, ages, integrated V magnitudes, distance moduli, reddenings, and bolometric corrections for the globular clusters listed in Tables 2 and 6.

Cluster	[M/H] ^a	age ^b [10 ⁹ yr]	V_i^c [mag]	$(m - M)_V^d$ [mag]	E_{B-V}^d [mag]	BC_V^e [mag]	Fraction of HB stars ^f		
							f_{RHB}	f_{BHB}	f_{EHB}
NGC 104	-0.76	13.1	4.01	13.37	0.04	-0.53	1.00	0.00	0.00
NGC 1851	-1.18	10.0	7.16	15.47	0.02	-0.41	0.64	0.36	0.00
NGC 5139	-1.64	11.5	3.85	13.94	0.12	-0.38	0.06	0.71	0.23
NGC 5272	-1.50	11.4	6.36	15.07	0.01	-0.38	0.32	0.68	0.00
NGC 5904	-1.33	10.6	5.58	14.46	0.03	-0.40	0.21	0.79	0.00
NGC 5986	-1.63	12.2	7.46	15.96	0.28	-0.38	0.00	0.91	0.09
NGC 6121	-1.18	12.5	5.77	12.82	0.35	-0.43	0.39	0.61	0.00
NGC 6205	-1.58	11.6	5.82	14.33	0.02	-0.38	0.00	0.70	0.30
NGC 6254	-1.57	11.4	6.60	14.08	0.28	-0.38	0.00	1.00	0.00
NGC 6397	-1.99	12.7	6.20	12.37	0.18	-0.37	0.00	1.00	0.00
NGC 6656	-1.70	12.7	5.08	13.60	0.34	-0.38	0.00	0.73	0.27
NGC 6712	-1.02	12.0	8.04	15.60	0.45	-0.44	0.85	0.15	0.00
NGC 6723	-1.10	13.1	7.03	14.84	0.05	-0.44	0.58	0.42	0.00
NGC 6752	-1.55	11.8	5.32	13.13	0.04	-0.38	0.00	0.72	0.28
NGC 6779	-2.00	13.7	8.17	15.68	0.26	-0.37	0.00	1.00	0.00
NGC 7078	-2.33	12.9	6.32	15.39	0.10	-0.35	0.10	0.90	0.00
NGC 7099	-2.33	12.9	7.35	14.64	0.03	-0.35	0.00	1.00	0.00

Notes. ^(a) Carretta et al. (2009) ^(b) (Marín-Franch et al. 2009, for NGC 6712 the age is taken from Paltrinieri et al. (2001)) ^(c) van den Bergh et al. (1991) ^(d) (Harris 1996, 2010 edition) ^(e) Worthey (1994) ^(f) The fraction of RHB, BHB, and EHB stars populating the HB (f_{RHB} , f_{BHB} , and f_{EHB} , respectively) of each cluster have been derived from the The Hubble Space Telescope UV Legacy Survey of Galactic Globular Clusters (Piotto et al. 2015; Soto et al. 2017), with the exception of ω Cen and NGC 6712, which are not part of the survey. For NGC 6712, which lacks an EHB, the RHB/BHB fractions were derived from the HB ratio presented by Paltrinieri et al. (2001), while the EHB, BHB, and RHB fractions for ω Cen were derived from Castellani et al. (2007) and Calamida et al. (2017).

We now wish to compare the number of observed post-AGB stars with expectations from stellar evolution models. In the absence of a detailed study of the distribution of stars in the HB of each cluster it is not possible to perform detailed synthetic population simulations for each cluster. However, using the available information from the HST UV Legacy Survey of Galactic Globular Clusters (Piotto et al. 2015; Soto et al. 2017) we estimated the fractions of stars populating the red HB (**RHB**),

BHB, and EHB, based on the HB morphology in the $V, V - I$ colour-magnitude diagram (see Table 7 for results). Using these numbers, we estimated how many post-AGB stars should evolve from the RHB, BHB, and EHB in each cluster.

The post-AGB evolutionary models computed for this work are an extension of the models presented by Miller Bertolami (2016). The models were computed for values of $[M/H] = -1, -1.5, -2$ and -2.3 under the assumption of a scaled-solar mix-

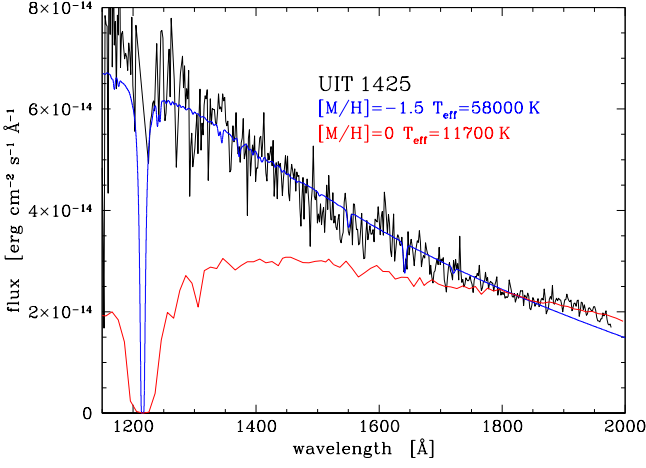


Fig. 4. IUE spectrum for NGC 5139–UIT1425 together with model spectra for $[M/H] = -1.5$ (blue, $T_{\text{eff}} = 58\,000\text{ K}$) and $[M/H] = 0$ (red, $T_{\text{eff}} = 11\,700\text{ K}$). The model spectra were red-denied by $E_{B-V} = 0.13$, aligned to a radial velocity of $+232\text{ km s}^{-1}$, and scaled to the observed flux between 1800 \AA and 1900 \AA . A hot star is clearly needed to reproduce the observed UV flux.

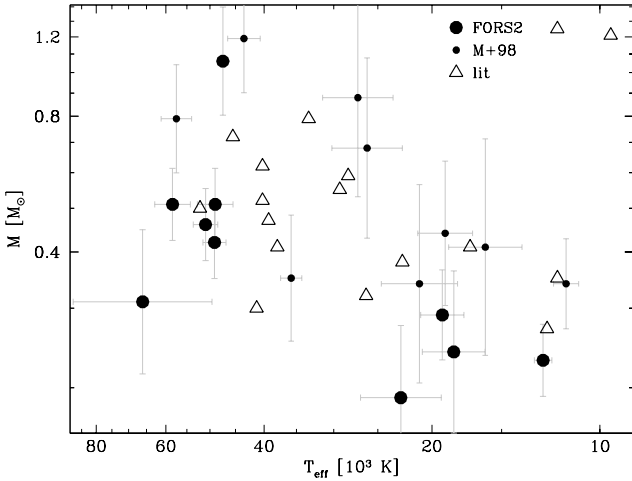


Fig. 5. Effective temperatures and masses for the hot UV-bright stars in globular clusters. For stars hotter than $40\,000\text{ K}$, we show the results obtained with model spectra with $[M/H] = +1$.

ture (Grevesse & Sauval 1998). The helium-metallicity relation was taken as in Miller Bertolami (2016), that is, $Y = 0.245 + 2 \times Z$. The initial masses of the models were chosen to correspond to ages between 11.5 to 12 Gyr. The higher or lower ages of some

Table 8. Initial parameters of the stellar evolution models

$[M/H]$	M_{ZAMS} [M_{\odot}]	Z_{ZAMS}	Y_{ZAMS}	X_{ZAMS}
-1.0	0.85	0.00172	0.24844	0.74984
-1.5	0.83	0.000548	0.246096	0.753356
-2.0	0.82	0.000174	0.245348	0.754478
-2.3	0.82	0.000087	0.245174	0.754739

Table 9. Number of expected hot post-AGB UV-bright stars with $\log L/L_{\odot} > 2.65$ and $80\,000\text{ K} > T_{\text{eff}} > 7000\text{ K}$ ($N_{\text{exp}}^{\text{post-AGB}}$) for the various clusters compared with the actual number of post-AGB stars in each cluster ($N_{\text{obs}}^{\text{post-AGB}}$).

Cluster	$N_{\text{obs}}^{\text{post-AGB}}$	$[M/H]_{\text{tracks}}$	$N_{\text{exp}}^{\text{post-AGB}}$
NGC 104	1	-1.00	0.08 – 0.65
NGC 1851	1	-1.00	0.15 – 1.04
NGC 5139	5	-1.50	1.31 – 13.58
NGC 5272	1	-1.50	0.27 – 1.48
NGC 5904	1	-1.50	0.38 – 2.11
NGC 5986	1	-1.50	0.61 – 4.29
NGC 6121	1	-1.00	0.19 – 1.32
NGC 6205	1	-1.50	0.23 – 2.71
NGC 6254	1	-1.50	0.26 – 1.44
NGC 6397	1	-2.00	0.07 – 0.26
NGC 6656	2	-1.50	0.59 – 6.65
NGC 6712	2	-1.00	0.14 – 0.98
NGC 6723	2	-1.00	0.12 – 0.83
NGC 6752	0	-1.50	0.13 – 1.48
NGC 6779	1	-2.00	0.29 – 1.13
NGC 7078	2	-2.30	1.04 – 3.71
NGC 7099	0	-2.30	0.17 – 0.64

of the globular clusters (see Table 7) are no problem because age does not influence the mass of the helium core at the time of the helium core flash, nor the following evolution. It might affect the mass of the hydrogen-rich envelope, but this mass is varied artificially in our models anyway to populate the whole horizontal branch. The corresponding initial parameters for the stellar evolution sequences are shown in Table 8. Different mass loss was applied to each model before the zero-age horizontal branch (ZAHB) in order to obtain different masses at the ZAHB and a complete coverage of the horizontal branch (from the RHB to the EHB) and post-HB evolution (see Table B.1 for details). Convective boundary mixing at all evolutionary stages and mass loss on the AGB were also adopted as in Miller Bertolami (2016). Figure 6 shows the atmospheric parameters derived in Sect. 4 compared to the evolutionary tracks. The evolutionary stage derived from this comparison can be found in Table 2. The stars are colour-coded by their helium abundance because this helps to identify the evolutionary status of a star. Significantly sub-solar helium abundances due to diffusion are known for HB stars hotter than about $11\,000\text{ K}$. The diffusion patterns are erased once convection starts in the atmosphere as the star evolves towards cooler temperatures. A low helium abundance is therefore unlikely for stars that ascended the AGB (even if only partially). Fig. 6 shows that helium-poor stars are found along post-(E)HB tracks and not along post-(e)AGB tracks. Helium-rich stars, on the other hand, are found only along the post-AGB tracks (except for the white dwarf merger).

In order to compare the stellar evolution models with the observed number of stars, we adopted the evolutionary flux method (see Greggio & Renzini 2011 for details). This method assumes that the late evolutionary stages are much shorter than the main-sequence evolution and that the number of “dying stars” can be equated to the number of stars leaving the main sequence. Under these assumptions, the number of stars N_k in a simple stellar population at each evolutionary stage k is given by

$$N_k = B \times L_{\text{total}} \times t_k, \quad (4)$$

where t_k is the duration of the evolutionary stage k , L_{total} is the total luminosity of the stellar population, and B stands for the specific evolutionary flux. For old stellar populations, like

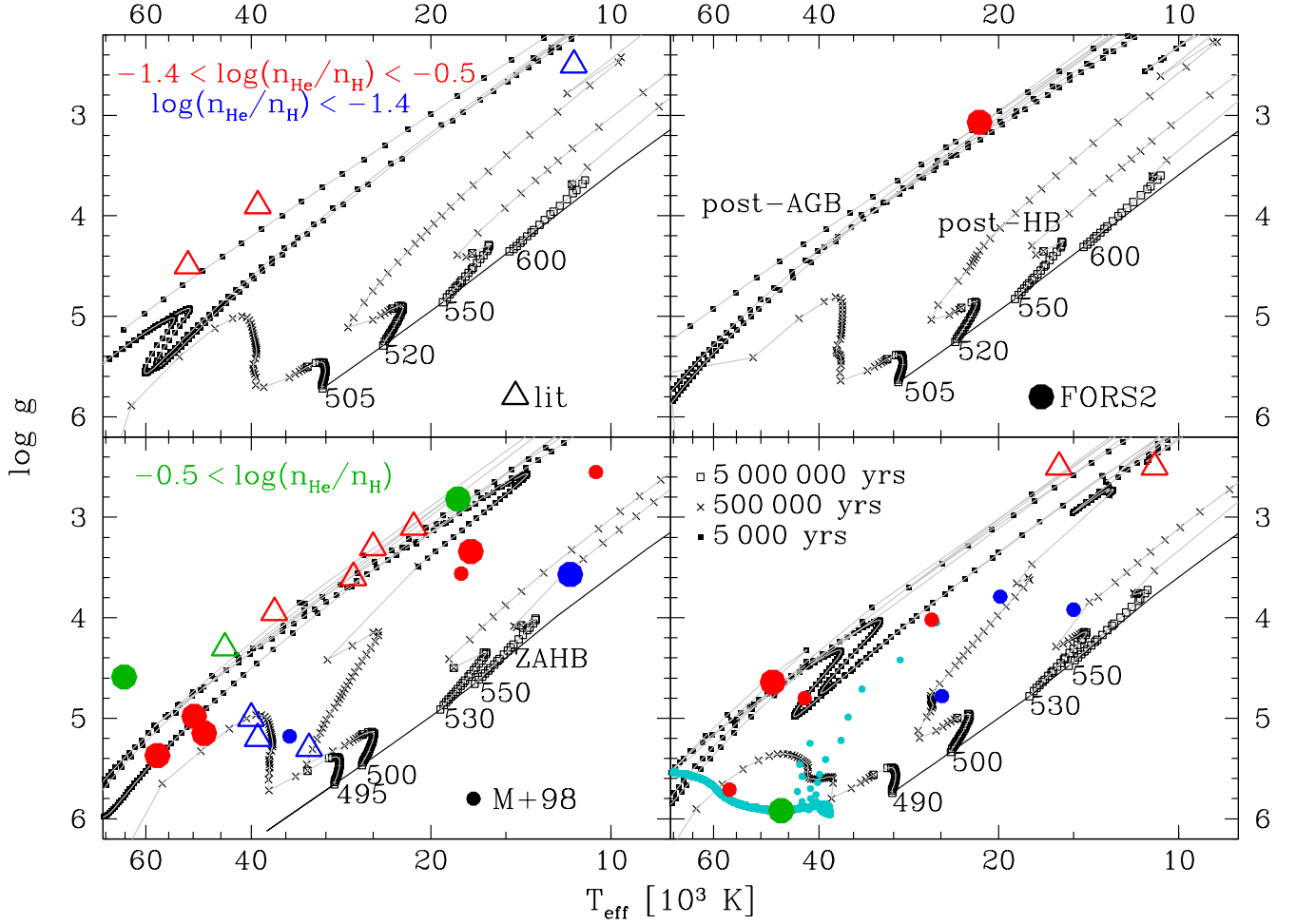


Fig. 6. Effective temperatures and surface gravities for the hot UV -bright stars in globular clusters. For stars hotter than 40 000 K, we show the results obtained with model spectra with $[M/H] = +1$. Stars from the literature without helium abundance are assumed to have solar abundance. The panels show the metallicity bins -2.3 (top left), -2 (top right), -1.5 (bottom left), and -1.0 (bottom right). The symbols along the tracks mark constant time steps. The cyan symbols mark time steps of 50 000 years along the white dwarf merger track from Zhang & Jeffery (2012).

the globular clusters studied in this work, we can approximate $B \approx 2 \times 10^{-11}$ stars per year and per solar luminosity (see Greggio & Renzini 2011 for details). In our case, we are interested in the time spent in the region of the Hertzsprung-Russell (**HR**) diagram where we would observe them as hot UV-bright post-AGB stars. We define the region in the HR diagram corresponding to hot UV-bright post-AGB stars detected in optical colours as that defined by $\log L/L_{\odot} > 2.65$ and $4.9 < \log T_{\text{eff}} < 3.845$ (grey zone in Fig. 7). Each computed track casts a timescale t corresponding to the time spent in that part of the HR diagram. With the parameters shown in Table 7 and with Eq. 4, we can compute for each cluster the expected numbers N^t predicted by each track t of a similar metallicity. It should be emphasized that Eq. 4 assumes that the whole cluster population evolved through that specific track k . Each post-HB track computed for the cluster metallicity gives a different expected number N_k (Eq. 4), and the actual number of expected post-HB stars will depend on the frequency with which each specific track is followed in each cluster. Lacking a better char-

acterization of the HB demographics, we can split the HB into the RHB, BHB, and EHB and then estimate the number of stars evolving from the RHB, BHB, or EHB using the relative populations of the RHB, BHB, and EHB in each cluster² (f_{RHB} , f_{BHB} , and f_{EHB} respectively, see Table 7). Using all sequences evolving from the RHB, BHB, or EHB, we obtain a range of expected numbers for hot post-AGB stars evolving from each part of the HB (N^{RHB} , N^{BHB} , or N^{EHB} , respectively). The actual range of expected UV-bright stars in the post-AGB region of the HR diagram (N) of a given cluster is then estimated as

$$N = f_{\text{EHB}} \cdot N^{\text{EHB}} + f_{\text{BHB}} \cdot N^{\text{BHB}} + f_{\text{RHB}} \cdot N^{\text{RHB}}. \quad (5)$$

The resulting ranges of expected numbers for each cluster are shown in Table 9. We excluded NGC 2808 from this investigation because we know that several luminous hot UV-bright stars are not included in our study (Jain et al. 2019). Overall,

² The lifetimes on the HB are not strongly affected by the effective temperature of the models, therefore this is a decent approximation.

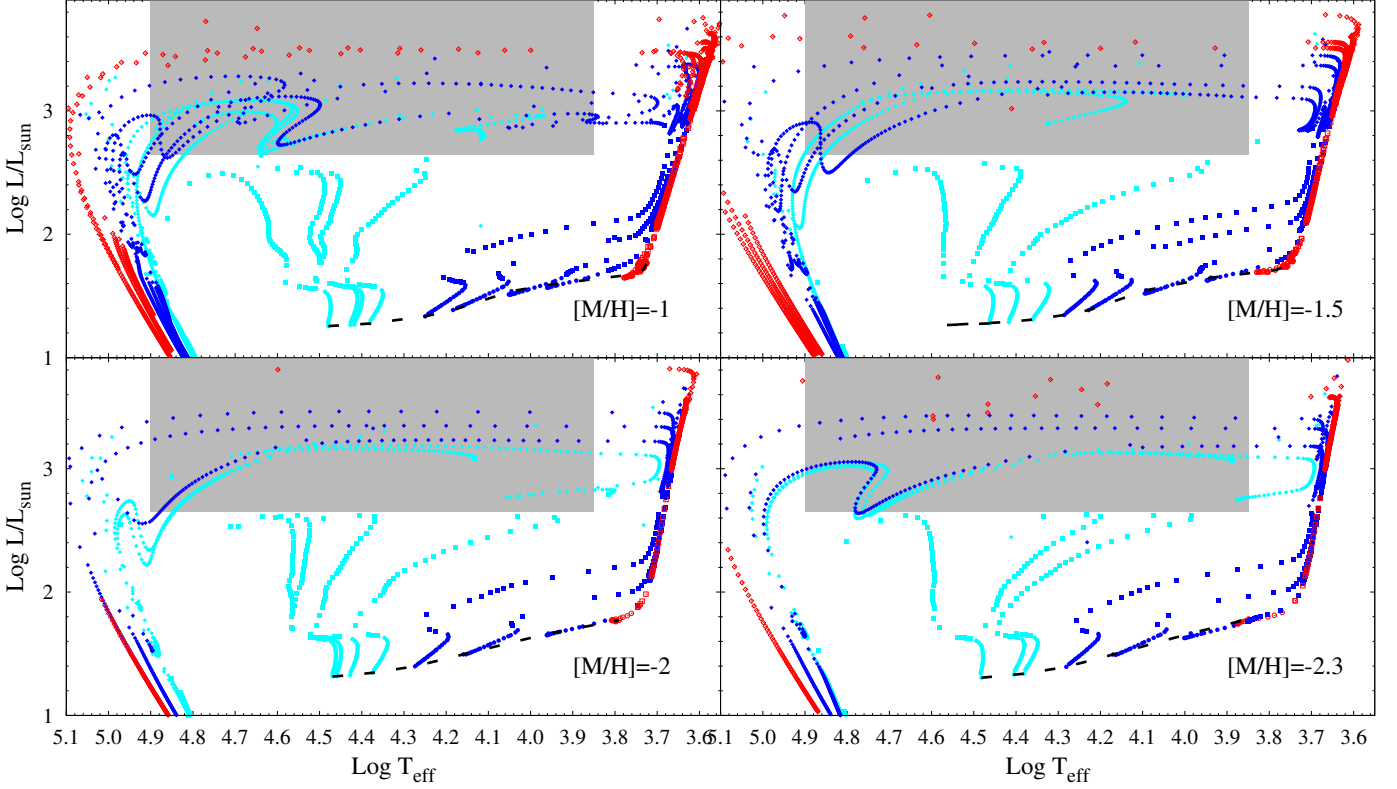


Fig. 7. Stellar evolution sequences computed for the present work (see Table B.1 for details). Black circles indicate the location of the HB and are plotted with a time step of 5 Myr, while squares and diamonds indicate the post-HB evolution with time steps of 0.5 Myr and 5 kyr, respectively. Cyan, blue, and red symbols indicate the sequences that populate the extreme, blue, and red parts of the HB. The gray region marks the parameter space of the hot post(-early) AGB stars in Table 9.

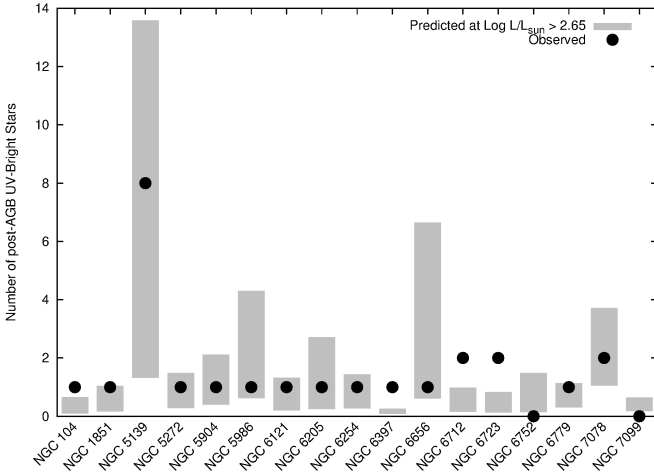


Fig. 8. Numbers of predicted (grey bars) and spectroscopically confirmed (black dots) hot post(-early) AGB stars in globular clusters.

the agreement between the number of post-AGB stars estimated ($N_{\text{exp}}^{\text{post-AGB}}$, fourth column in Table 9) and the observed number of post-AGB stars ($N_{\text{obs}}^{\text{post-AGB}}$, second column in Table 9) in each cluster is good (see also Fig. 8). In 11 out of 17 cases ($\approx 65\%$) the observed number of stars lies within the computed range, while in 3 other cases (NGC 104, NGC 6752, and NGC 7099)

the observed number is just an integer number next to the expected range. A more significant discrepancy is observed for NGC 6712 and NGC 6723, where the upper boundary of the predicted ranges is a factor ≈ 2 lower than the observed number. An even larger discrepancy is observed for NGC 6397, for which the largest predicted number is about four times smaller than the observed one. In these three cases, the observed value is higher than the predicted ones, but a word of caution is in order. We have preselected for our sample those clusters that do harbour hot UV-bright stars. It is therefore possible that our clusters are biased to larger post-AGB numbers. Given the low number of the expected post-AGB stars and the fact that the observed number is necessarily an integer, it is difficult to point to this discrepancy as a discrepancy with the stellar evolution models. A full comparison of all clusters searched for hot UV-bright stars is required for firmer conclusions.

8. Conclusions

Our results first confirm that spectroscopic observations of UV-bright stars are required to verify their evolutionary status, as is shown by the cases of NGC 7099–UVBS2 and NGC 6121–UVBS2. The need for metal-rich model spectra in the analysis of hot evolved stars has been reported elsewhere (Latour et al. 2015), and we can confirm that additional opacities are required to reproduce the He I and He II lines simultaneously and the UV spectra. This should be kept in mind when

the contribution of hot post-AGB stars to the UV flux of evolved populations is estimated.

We find general agreement for the number of observed hot post-AGB stars compared to predictions from evolutionary theory, although the numbers per cluster are low (at most two, except for ω Cen, which has five). Some discrepancies are observed in the clusters NGC 6397, NGC 6712, and NGC 6723, which show somewhat larger numbers than expected from the models. Because of the small-number statistics nature of the comparison, it is unclear, however, whether this is due to a problem with the models or a result of the way the sample was preselected. In order to improve our constraints on low-mass post-AGB stellar evolution models, the number of studied globular clusters needs to be increased. When the full set of 78 globular clusters with UV-imaging is studied, it will be possible to combine clusters with similar metallicities and HB morphologies to improve the number statistics in the comparisons.

Acknowledgements. We are grateful to Nicole Reindl, who made her co-added spectrum of SDSS J155610.40+254640.3 and its model spectrum available to us. We thank Simon Jeffery for the merger track and his explanations of the merger behaviour. We appreciate the anonymous referee's comments that improved the readability and clarity of this paper substantially. M.M.M.B. is partially supported through ANPCyT grant PICT-2016-0053 and MinCyT-DAAD bilateral cooperation program through grant DA/16/07. This research has made use of NASA's Astrophysics Data System Bibliographic Services and of the VizieR catalogue access tool, CDS, Strasbourg, France. The original description of the VizieR service was published in Ochsenbein et al. (2000). Some of the data presented in this paper were obtained from the Mikulski Archive for Space Telescopes (MAST). STScI is operated by the Association of Universities for Research in Astronomy, Inc., under NASA contract NAS5-26555.

References

- Alves, D. R., Bond, H. E., & Onken, C. 2001, *AJ*, 121, 318
- Appenzeller, I., Fricke, K., Fürtig, W., et al. 1998, *The Messenger*, 94, 1
- Arp, H. C. & Melbourne, W. G. 1959, *AJ*, 64, 28
- Bellini, A., Piotto, G., Bedin, L. R., et al. 2009, *A&A*, 493, 959
- Bergeron, P., Saffer, R. A., & Liebert, J. 1992, *ApJ*, 394, 228
- Bohlin, R. C. & Bianchi, L. 2018, *AJ*, 155, 162
- Bond, H. E. 2015, *AJ*, 149, 132
- Brown, T. M., Lanz, T., Sweigart, A. V., et al. 2012, *ApJ*, 748, 85
- Brown, T. M., Smith, E., Ferguson, H. C., et al. 2008, *ApJ*, 682, 319
- Buonanno, R., Buscema, G., Corsi, C. E., Iannicola, G., & Fusi Pecci, F. 1983, *A&AS*, 51, 83
- Buonanno, R., Caloi, V., Castellani, V., et al. 1986, *A&AS*, 66, 79
- Buzzoni, A., Cacciari, C., Fusi-Pecci, F., Buonanno, R., & Corsi, C. E. 1992, *A&A*, 254, 110
- Calamida, A., Strampelli, G., Rest, A., et al. 2017, *AJ*, 153, 175
- Carretta, E., Bragaglia, A., Gratton, R., D'Orazi, V., & Lucatello, S. 2009, *A&A*, 508, 695
- Castellani, V., Calamida, A., Bono, G., et al. 2007, *ApJ*, 663, 1021
- Charpinet, S., Van Grootel, V., Fontaine, G., et al. 2011, *A&A*, 530, A3
- Chayer, P., Dixon, W. V., Fullerton, A. W., Ooghe-Tabanou, B., & Reid, I. N. 2015, *MNRAS*, 452, 2292
- Constantino, T., Campbell, S. W., Christensen-Dalsgaard, J., Lattanzio, J. C., & Stello, D. 2015, *MNRAS*, 452, 123
- Cudworth, K. M. 1988, *AJ*, 96, 105
- de Boer, K. S. 1987, in *IAU Colloq. 95: Second Conference on Faint Blue Stars*, ed. A. G. D. Philip, D. S. Hayes, & J. W. Liebert, 95–104
- Dixon, W. V., Chayer, P., Latour, M., Miller Bertolami, M. M., & Benjamin, R. A. 2017, *AJ*, 154, 126
- Dixon, W. V., Chayer, P., Reid, I. N., & Miller Bertolami, M. M. 2019, *AJ*, 157, 147
- Dixon, W. V. D., Brown, T. M., & Landsman, W. B. 2004, *ApJ*, 600, L43
- Dixon, W. V. D., Davidsen, A. F., & Ferguson, H. C. 1994, *AJ*, 107, 1388
- Dixon, W. V. D., Davidsen, A. F., & Ferguson, H. C. 1995, *ApJ*, 454, L47
- Dorman, B., Rood, R. T., & O'Connell, R. W. 1993, *ApJ*, 419, 596
- Flower, P. J. 1996, *ApJ*, 469, 355
- Gaia Collaboration, Helmi, A., van Leeuwen, F., et al. 2018, *A&A*, 616, A12
- Gaspey, J. W., Demers, S., Moffat, A. F. J., & Shara, M. 1985, *ApJ*, 289, 326
- Greggio, L. & Renzini, A. 2011, *Stellar Populations. A User Guide from Low to High Redshift*
- Grevesse, N. & Sauval, A. J. 1998, *Space Sci. Rev.*, 85, 161
- Harrington, J. P. & Paltoglou, G. 1993, *ApJ*, 411, L103
- Harris, W. E. 1996, *AJ*, 112, 1487
- Heber, U. & Kudritzki, R. P. 1986, *A&A*, 169, 244
- Hubeny, I. & Lanz, T. 1995, *ApJ*, 439, 875
- Hubeny, I. & Lanz, T. 2017, *arXiv*, 1706.01859
- Jacoby, G. H., Morse, J. A., Fullton, L. K., Kwitter, K. B., & Henry, R. B. C. 1997, *AJ*, 114, 2611
- Jain, R., Vig, S., & Ghosh, S. K. 2019, *MNRAS*, 485, 2877
- Jasniewicz, G., de Laverny, P., Parthasarathy, M., Lèbre, A., & Thévenin, F. 2004, *A&A*, 423, 353
- Johnson, C. I., Pilachowski, C. A., Simmerer, J., & Schwenk, D. 2008, *ApJ*, 681, 1505
- Lane, R. R., Kiss, L. L., Lewis, G. F., et al. 2010, *MNRAS*, 406, 2732
- Lanz, T. & Hubeny, I. 2003, *ApJS*, 146, 417
- Lanz, T. & Hubeny, I. 2007, *ApJS*, 169, 83
- Latour, M., Chayer, P., Green, E. M., Irrgang, A., & Fontaine, G. 2018, *A&A*, 609, A89
- Latour, M., Fontaine, G., Green, E. M., & Brassard, P. 2015, *A&A*, 579, A39
- Lloyd Evans, T. 1974, *MNRAS*, 167, 393
- Marín-Franch, A., Aparicio, A., Piotto, G., et al. 2009, *ApJ*, 694, 1498
- Martin, D. C., Fanson, J., Schiminovich, D., et al. 2005, *ApJ*, 619, L1
- McDonald, I. & Zijlstra, A. A. 2015, *MNRAS*, 448, 502
- Miller Bertolami, M. M. 2016, *A&A*, 588, A25
- Milvang-Jensen, B., Noll, S., Halliday, C., et al. 2008, *A&A*, 482, 419
- Mochejska, B. J., Kaluzny, J., Thompson, I., & Pych, W. 2002, *AJ*, 124, 1486
- Moehler, S., Dabo, C. E. G., Boffin, H., et al. 2015, *The Messenger*, 159, 10
- Moehler, S., Dreizler, S., Lanz, T., et al. 2011, *A&A*, 526, A136
- Moehler, S., Heber, U., & Rupprecht, G. 1997, *A&A*, 319, 109
- Moehler, S., Landsman, W., & Napiwotzki, R. 1998, *A&A*, 335, 510
- Moehler, S., Modigliani, A., Freudling, W., et al. 2014, *A&A*
- Moehler, S. & Sweigart, A. V. 2006, *A&A*, 455, 943
- Moehler, S., Sweigart, A. V., Landsman, W. B., & Heber, U. 2000, *A&A*, 360, 120
- Monaco, L., Pancino, E., Ferraro, F. R., & Bellazzini, M. 2004, *MNRAS*, 349, 1278
- Mooney, C. J., Rolleston, W. R. J., Keenan, F. P., et al. 2004, *A&A*, 419, 1123
- Muthumariappan, C., Parthasarathy, M., & Ita, Y. 2013, *MNRAS*, 435, 606
- Napiwotzki, R., Green, P. J., & Saffer, R. A. 1999, *ApJ*, 517, 399
- Nardiello, D., Libralato, M., Piotto, G., et al. 2018, *MNRAS*, 481, 3382
- Ochsenbein, F., Bauer, P., & Marcout, J. 2000, *A&AS*, 143, 23
- Paltrinieri, B., Ferraro, F. R., Paresce, F., & De Marchi, G. 2001, *AJ*, 121, 3114
- Patat, F., Moehler, S., O'Brien, K., et al. 2011, *A&A*, 527, A91
- Piotto, G., King, I. R., Djorgovski, S. G., et al. 2002, *A&A*, 391, 945
- Piotto, G., Milone, A. P., Bedin, L. R., et al. 2015, *AJ*, 149, 91
- Poole, T. S., Breeveld, A. A., Page, M. J., et al. 2008, *MNRAS*, 383, 627
- Rauch, T., Heber, U., Hunger, K., Werner, K., & Neckel, T. 1991, *A&A*, 241, 457
- Rauch, T., Heber, U., & Werner, K. 2002, *A&A*, 381, 1007
- Reindl, N., Geier, S., Kupfer, T., et al. 2016, *A&A*, 587, A101
- Remillard, R. A., Canizares, C. R., & McClintock, J. E. 1980, *ApJ*, 240, 109
- Renzini, A. 1985, in *Horizontal-Branch and UV-Bright Stars*, ed. A. G. D. Philip, 19–29
- Rosenberg, A., Aparicio, A., Saviane, I., & Piotto, G. 2000, *A&AS*, 145, 451
- Saffer, R. A., Bergeron, P., Koester, D., & Liebert, J. 1994, *ApJ*, 432, 351
- Salaris, M., Cassisi, S., & Pietrinfermi, A. 2016, *A&A*, 590, A64
- Sandquist, E. L., Bolte, M., Langer, G. E., Hesser, J. E., & de Oliveira, C. M. 1999, *ApJ*, 518, 262
- Sandquist, E. L., Gordon, M., Levine, D., & Bolte, M. 2010, *AJ*, 139, 2374
- Soto, M., Bellini, A., Anderson, J., et al. 2017, *AJ*, 153, 19
- Stecher, T. P., Cornett, R. H., Greason, M. R., et al. 1997, *PASP*, 109, 584
- Thompson, H. M. A., Keenan, F. P., Dufton, P. L., et al. 2007, *MNRAS*, 378, 1619
- van den Bergh, S., Morbey, C., & Pazder, J. 1991, *ApJ*, 375, 594
- Walker, A. R. 1992, *PASP*, 104, 1063
- Webbink, R. F. 1981, *ApJS*, 45, 259
- Weston, S., Napiwotzki, R., & Catalán, S. 2010, in *American Institute of Physics Conference Series*, Vol. 1273, American Institute of Physics Conference Series, ed. K. Werner & T. Rauch, 197–202
- Worthey, G. 1994, *ApJS*, 95, 107
- Yong, D., Meléndez, J., Cunha, K., et al. 2008, *ApJ*, 689, 1020
- Zhang, X. & Jeffery, C. S. 2012, *MNRAS*, 419, 452

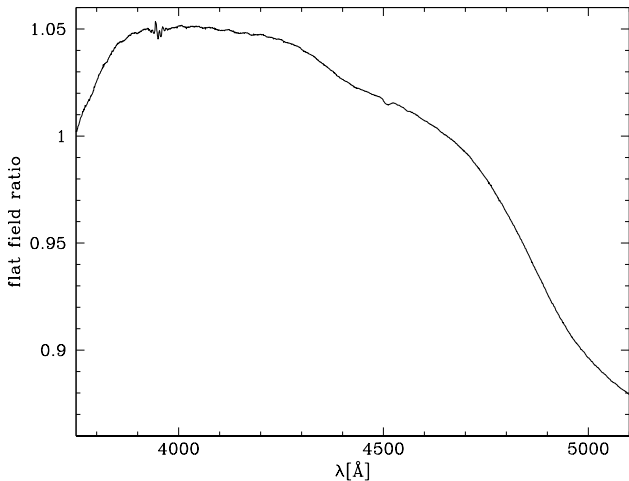


Fig. A.1. Ratio of the averaged wavelength-calibrated flat-field spectra observed with the LSS 0'5 slit and with a 5'' MOS slit at the position of the 0'5 long slit (both normalized by their median flux). The ratio shows clear large-scale variations of some 20%.

Appendix A: Flux calibration

GRIS_1200B is a volume-phase holographic grism. Its response therefore depends on the position of the slit along the dispersion axis. The best solution for a flux calibration is to take the flux standard star at the same place on the detector as the science spectrum. This is done for data taken with the long slit by creating a 5'' wide long slit with the slit blades of the MOS slitlets. For MOS observations with distributed slitlets, this would require taking several flux standard star observations, which is not feasible in service mode.

To correct the response derived from standard stars taken at different positions than the science targets, we made use of the fact that the varying response is seen also in the spectral energy distribution of the screen flat fields taken for the MOS data (see Milvang-Jensen et al. 2008 and Moehler et al. 2015 for a more detailed description). Therefore we took the ratio of the wavelength-calibrated master screen flat and normalized master flat and averaged it along the slit. Then we divided the extracted standard star spectra and the extracted science spectra by their flat-field spectra. This procedure will of course introduce the lamp spectrum into these spectra, but as long as the lamp spectrum does not change, this can be corrected for with the response curve.

During this exercise we noted three potential problems:

1. The narrow-slit flat fields taken until June 22, 2012, show two emission lines at about 3944.2 Å and 3961.8 Å. The lines are not visible in the 5'' flat fields taken for the standard stars. The smoothing of the master screen flat along the dispersion axis will smear out these lines to a radius of at least ± 10 pixels or ± 7 Å (relative to the peak position). We therefore did not use these regions in our later analysis.
2. Between June 22 and July 22, 2012, the spectral energy distribution of the flat-field lamps changed.
3. Even between flat fields taken within 30 minutes of each other, the spectral energy distribution changed by some 20% (see Fig. A.1).

All extracted spectra (science and standard stars) were corrected for atmospheric extinction using the extinction coefficients of Patat et al. (2011).

In order to have a finely sampled response, we used observations of EG 274 (April 20, 2012) and Feige 110 (June 22, 2012), for which finely sampled reference spectra exist (Moehler et al. 2014). We determined the radial velocity of the observed spectrum using the H δ line, aligned the noise-free reference spectrum to the same radial velocity, and resampled it to the same wavelength steps as the observed spectrum. Then we computed the ratio of the observed extinction-corrected standard star spectrum and the resampled reference spectrum. This ratio showed small residuals at the positions of strong stellar lines, which we masked when we fit a smoothed spline to the ratio. This fit was then used to flux-calibrate the extinction-corrected science data.

As noted above, the spectral energy distribution of the flat fields changed between June 22 and July 22, 2012. Only long-slit spectra were taken after June 22. We therefore decided to use the flat-field spectrum taken for the long slit on June 14, 2012, to correct all long-slit spectra. This procedure allowed us to use the standard star observed on June 22, 2012 also for data from July. In principle, the long-slit spectra do not even need to be corrected if a standard star was observed at the same position (as is the case for Feige 110). However, the smoothed flat-field spectra show some variations in detector response at the blue end that are hard to fit without a high risk of fitting noise in the response. The division by the flat-field spectra is therefore useful beyond correcting the position dependency of the response.

In order to deal with the short-term variations of the flat-field lamp we used the same flat-field spectrum for the standard star taken at the position of the LSS 0'5 slit and all science data taken with the long slit. For the MOS data we could not use the same flat field for science data and standard star because they were observed at different positions on the CCD.

Appendix B: Details of the stellar evolution sequences

Table B.1. Description of the stellar evolution sequences computed for this work. TP-AGB stands for thermally pulsing AGB, (V)LTP for (very) late thermal pulse

M_{ZAHB} [M_{\odot}]	$T_{\text{eff,ZAHB}}$ [K]	$\log g_{\text{ZAHB}}$ [cm s^{-2}]	HB location	post-HB behavior	M_{final} [M_{\odot}]
[M/H]= -1, Age= 12 Gyr, $M_{\text{ZAMS}} = 0.85M_{\odot}$					
0.490	30138	5.74	EHB	post-EHB, no thermal pulses	0.490
0.494	26706	5.52	EHB	1 thermal pulse (like a LTP)	0.493
0.495	26152	5.49	EHB	1 thermal pulse (like a LTP)	0.495
0.500	24040	5.34	EHB	2 thermal pulses (like a LTP)	0.496
0.530	17770	4.78	BHB	post-EAGB, 2 thermal pulses (like a LTP)	0.499
0.550	15264	4.48	BHB	TP-AGB + LTP	0.504
0.580	11097	3.80	BHB	TP-AGB + LTP	0.513
0.600	8815	3.35	BHB	TP-AGB	0.518
0.650	5724	2.56	RHB	TP-AGB +LTP	0.528‡
0.700	5484	2.50	RHB	TP-AGB	0.537
0.750	5392	2.47	RHB	TP-AGB	0.545
0.850	5315	2.46	RHB	TP-AGB	0.555
[M/H]= -1.5, Age= 11.7 Gyr, $M_{\text{ZAMS}} = 0.83M_{\odot}$					
0.495	29013	5.66	EHB	post-EHB, no thermal pulses	0.495
0.500	26116	5.47	EHB	1 thermal pulse (like a LTP)	0.499
0.510	22942	5.23	EHB	post-EAGB, 1 thermal pulse (like a LTP)	0.500
0.530	19297	4.91	BHB	post-EAGB, 1 thermal pulse (like a LTP)	0.501
0.550	16897	4.66	BHB	TP-AGB + LTP	0.505
0.600	12354	3.99	BHB	TP-AGB + LTP	0.519
0.650	8670	3.31	BHB	TP-AGB + VLTP	0.525‡
0.700	6105	2.67	RR Lyr	TP-AGB + LTP	0.540‡
0.750	5700	2.54	RR Lyr	TP-AGB + LTP	0.550‡
0.830	5542	2.50	RHB	TP-AGB	0.557
[M/H]= -2, Age= 11.8 Gyr, $M_{\text{ZAMS}} = 0.82M_{\odot}$					
0.505	29455	5.65	EHB	post-EHB, no thermal pulses	0.505
0.506	28773	5.61	EHB	post-EHB, no thermal pulses	0.506
0.510	26760	5.48	EHB	1 thermal pulse (like a LTP)	0.509
0.520	23648	5.26	EHB	post-EAGB, 1 thermal pulse (like a LTP)	0.510
0.550	18774	4.83	BHB	post-EAGB, 1 thermal pulse (like a LTP)	0.513
0.600	14431	4.31	BHB	TP-AGB	0.525
0.700	9064	3.40	BHB	TP-AGB	0.547
0.820	6164	2.69	RR Lyr	TP-AGB	0.557
[M/H]= -2.3, Age= 11.7 Gyr, $M_{\text{ZAMS}} = 0.82M_{\odot}$					
0.505	30346	5.72	EHB	post-EHB, no thermal pulses	0.505
0.515	25384	5.39	EHB	1 thermal pulse (like a LTP)	0.511
0.520	24034	5.29	EHB	post-EAGB, 1 thermal pulse (like a LTP)	0.512
0.550	19090	4.86	BHB	TP-AGB	0.513
0.600	14787	4.35	BHB	TP-AGB+VLTP	0.510
0.700	9681	3.51	BHB	TP-AGB	0.546
0.820	7967	2.92	RR Lyr	TP-AGB	0.570

‡ These sequences ended highly H-deficient due to burning or dilution of the H-rich envelope during the last He-shell flash.